Centennial Variations of the Global Monsoon Precipitation in the Last Millennium: Results from ECHO-G Model

JIAN LIU,* BIN WANG,+,# QINGHUA DING,+ XUEYUAN KUANG,* WILLIE SOON,@ AND EDUARDO ZORITA&

*State Key Laboratory of Lake Science and Environment, Nanjing Institute of Geography and Limnology, Chinese Academy of Sciences, Nanjing, China
+ Department of Meteorology, and International Pacific Research Center, University of Hawaii at Manoa, Honolulu, Hawaii
# CPEO, Ocean University of China, Qingdao, China
@ Harvard-Smithsonian Center for Astrophysics, Cambridge, Massachusetts
& Institute for Coastal Research, GKSS Research Center, Geesthacht, Germany

(Manuscript received 29 November 2007, in final form 3 September 2008)

ABSTRACT

The authors investigate how the global monsoon (GM) precipitation responds to the external and anthropogenic forcing in the last millennium by analyzing a pair of control and forced millennium simulations with the ECHAM and the global Hamburg Ocean Primitive Equation (ECHO-G) coupled ocean–atmosphere model. The forced run, which includes the solar, volcanic, and greenhouse gas forcing, captures the major modes of precipitation climatology comparably well when contrasted with those captured by the NCEP reanalysis. The strength of the modeled GM precipitation in the forced run exhibits a significant quasi-bicentennial oscillation. Over the past 1000 yr, the simulated GM precipitation was weak during the Little Ice Age (1450–1850) with the three weakest periods occurring around 1460, 1685, and 1800, which fell in, respectively, the Spörer Minimum, Maunder Minimum, and Dalton Minimum periods of solar activity. Conversely, strong GM was simulated during the model Medieval Warm Period (ca. 1030–1240). Before the industrial period, the natural variations in the total amount of effective solar radiative forcing reinforce the thermal contrasts both between the ocean and continent and between the Northern and Southern Hemispheres resulting in the millennium-scale variation and the quasi-bicentennial oscillation in the GM index. The prominent upward trend in the GM precipitation occurring in the last century and the notable strengthening of the global monsoon in the last 30 yr (1961–90) appear unprecedented and are due possibly in part to the increase of atmospheric carbon dioxide concentration, though the authors' simulations of the effects from recent warming may be overestimated without considering the negative feedbacks from aerosols. The simulated change of GM in the last 30 yr has a spatial pattern that differs from that during the Medieval Warm Period, suggesting that global warming that arises from the increases of greenhouse gases and the input solar forcing may have different effects on the characteristics of GM precipitation. It is further noted that GM strength has good relational coherence with the temperature difference between the Northern and Southern Hemispheres, and that on centennial time scales the GM strength responds more directly to the effective solar forcing than the concurrent forced response in global-mean surface temperature.

1. Introduction

Monsoon climate varies on several characteristic time scales in addition to fluctuations of random origin. In the last two decades, significant progress has been made in the study of monsoon variability on intraseasonal, interannual, interdecadal, and orbital time scales of tens of thousands of years. A review of recent progresses in the understanding of Asian monsoon variability has been summarized in Wang (2006). However, the centennial-scale variability of the global monsoon system has been considerably less studied. On time scale of centuries, the internal feedback processes that control the interannual-to interdecadal-scale variations become less important; in the meantime, the persistent, external forcing from centennial-scale variations in solar radiation, when viewed from the perspective of local and regional spatial domains,

Corresponding author address: Dr. J. Liu, State Key Laboratory of Lake Science and Environment, Nanjing Institute of Geography and Limnology, Chinese Academy of Sciences, 73 East Beijing Road, Nanjing 210008, China.
E-mail: jianliu@niglas.ac.cn

DOI: 10.1175/2008JCLI2353.1

may be considerably stronger and more effective than the effect of internal feedback. Both the nature and cause of the centennial-scale variability are largely not known and understudied.

In contrast to numerous studies on the global-mean temperature, we focus on global monsoon precipitation in this study. Why are we particularly concerned with the global monsoon precipitation? The monsoon rainfall provides water resources to about two-thirds of the world's population, so any improved knowledge on its variation will be of great societal importance. Monsoon precipitation is also of scientific importance as it is the key variable of the global water cycle and it provides a critical heat source for driving atmospheric circulation.

What is the global monsoon? Previous studies have mostly focused on the monsoon changes in specific regions because of considerable regionality of the monsoon variations. Yet regional monsoons are coordinated by the same annual cycle of the solar forcing and their variations are interrelated. Trenberth et al. (2000) argued that the conservation of atmospheric mass, moisture, and energy spread over global domain with exchanges in the lower boundary. They have defined the global monsoon system as a global-scale overturning circulation that varies annually. Wang (1994) first attempted to delineate the global monsoon regime using outgoing longwave radiation data as the proxy for deep convection and precipitation. Wang and Ding (2006) further demarcated a global monsoon (GM) precipitation domain based on characteristics of monsoon precipitation and examined the trends of the GM rainfall over land using four sets of rain gauge precipitation datasets compiled for the period 1948–2003. But how the GM changes on multidecadal to millennial time scales and what mechanisms are responsible for them remain poorly studied.

One of the major roadblocks for studying GM variability on centennial or millennial scale is the lack of direct observations, especially on the global scale. To make progress, we consider numerical simulations with atmosphere–ocean coupled climate models for the last millennium. These simulations may provide useful surrogate datasets for analyzing and understanding any changes of GM precipitation on multidecadal to centennial time scales. These kinds of simulations have been constructed using a wide variety of climate models with different levels of complexity, including the second climate configuration of the Met Office Unified Model (HadCM2; Johns et al. 1997), Geophysical Fluid Dynamics Laboratory (GFDL) model (Manabe and Stouffer 1993; Stouffer et al. 2000), Commonwealth Scientific and Industrial Research Organisation (CSIRO) model (Vimont et al. 2002), ECHAM and the global Hamburg Ocean Primitive Equation (ECHO-G) model (Rodgers et al. 2004; Min et al. 2005a,b; Wagner et al. 2005), and Meteorological Research Institute Coupled General Circulation Model, version 2.2 (MRI CGCM2.2) model (Kitoh 2006) for control simulations; and the Climate and Biosphere Model (CLIMBER)-2 model (Bauer et al. 2003), ECHO-G model (Zorita et al. 2003; González-Rouco et al. 2003; Zorita et al. 2005; Gouirand et al. 2007a,b), ocean–atmosphere–sea ice model of intermediate complexity de Bilt–coupled large-scale ice–ocean (ECBilt–CLIO) model (Goosse et al. 2005), Model for the Assessment of Greenhouse-Gas Induced Climate Change (MAGICC) model (Osborn et al. 2006), ECHAM4/Ocean Isopycnal Model (OPYC3; Stendel et al. 2006), third climate configuration of the Met Office Unified Model (HadCM3; Tett et al. 2007), and National Center for Atmospheric Research Climate System Model (NCAR CSM; Mann et al. 2005b; Ammann et al. 2007) for forced simulations of the past millennium or past half millennium.

Based on these model results, the internal variability of temperature, precipitation, mean sea level pressure, and major modes of climate variation such as the North Atlantic Oscillation (NAO), ENSO, and Indian monsoon have been discussed (Min et al. 2005a,b; Zorita et al. 2003; Kitoh 2006). Variabilities on interannual, decadal, multidecadal, and centennial time scales under natural and anthropogenic forcing have also been examined in terms of surface and subsurface temperatures (Stouffer et al. 2000; Beltrami et al. 2006; González-Rouco et al. 2003; Zorita et al. 2005; Wagner et al. 2005; Osborn et al. 2006). Both model–model comparison (Goosse et al. 2005; Osborn et al. 2006) and model–data comparison (Liu et al. 2005; Beltrami et al. 2006) among convenient indexes like SST, ENSO, NAO, and Arctic Oscillation (AO; Vimont et al. 2002; Rodgers et al. 2004; Goosse et al. 2005; Gouirand et al. 2007a,b) have been performed in order to assess the reality and robustness of models' simulations. Roles of centennial-scale variations in solar activity (Wagner et al. 2001; Fleitmann et al. 2003; Weber et al. 2004; Wiles et al. 2004; Holzkämper et al. 2004; Delmonte et al. 2005; Lim et al. 2005; Wang et al. 2005; Haltia-Hovi et al. 2007) and changes between volcanic pulse forcing (Crowley 2000; Goosse and Renssen 2004; Mann et al. 2005a) have also been recently investigated and argued through a combination of paleo–proxy data analyses and climate modelings.

But how does the GM rainfall respond to natural and anthropogenic forcing in the last millennium? How do the spatial patterns of GM precipitation anomalies differ between the warm and cold periods in the millennium? How do the changes of GM rainfall relate to the changes

of global temperature and interhemispheric temperature difference? These open questions will be explored here.

To study these questions, we first explore the performance of climate model (ECHO-G) in simulating annual mean and annual cycle of the precipitation in the global tropics and subtropics (section 2); next we define the global monsoon indexes (GMI) for the variability of global monsoon precipitation and its centennial-to-millennial-scale variability (section 3); the ECHO-G simulation clearly yielded the mock-up versions of the Medieval Warm Period (MWP), Little Ice Age (LIA), and Present Warm Period (PWP)—their durations in the model will be defined later. We will then compare the spatial structure of GM precipitation during the MWP, LIA, and PWP (section 4), and finally we discuss the forcing-response relationships between GMI and radiative forcings from changes in solar activity, volcanic eruptions, as well as atmospheric CO_2 and CH_4 concentration (section 5). Section 6 summarizes the main results of this paper.

2. Model and its validation

a. Model and simulation

The ECHO-G climate model (Legutke and Voss 1999) consists of the spectral atmospheric model ECHAM4 (Roeckner et al. 1996) and the Hamburg Ocean Primitive Equation global (HOPE-G) model (Wolff et al. 1997), both developed at the Max Planck Institute for Meteorology in Hamburg. The ECHAM4 is based on primitive equations with a mixed p-σ coordinate system. The model configuration used for these simulations has 19 vertical levels in the atmosphere and 20 levels in the ocean, and horizontal resolutions are approximately 3.75° (atmosphere) and 2.8° (ocean) in both latitudes and longitudes. The ocean model HOPE-G has a grid refinement in the tropical regions, where the meridional grid point separation reaches 0.5°. To enable the coupled model to sustain a simulated climate near to the real present-day climate with minimal drift, both heat and freshwater fluxes between the atmosphere and ocean are modified by adding a constant (in time) field of adjustment with net-zero spatial average (Roeckner et al. 1996; Wolff et al. 1997).

Two millennial integrations with the ECHO-G model will be analyzed here. One is the 1000-yr control simulation (CTL), which was generated using fixed external (annually cycling) forcing set to the present-day values (Zorita et al. 2003). This CTL experiment can simulate annual-to-decadal climate oscillations through the internal dynamics of the coupled climate system (Min et al. 2005a,b). The second simulation, named ERIK (covering the period 1000–1990), is forced by three external forcing factors (González-Rouco et al. 2003; von Storch et al. 2004; Zorita et al. 2005): solar variability (Crowley 2000; von Storch et al. 2004), greenhouse gas concentrations in the atmosphere including CO_2 and CH_4 (Blunier et al. 1995; Etheridge et al. 1996), and the effective radiative effects from stratospheric volcanic aerosols (Crowley 2000) for the period AD 1000–1990. The volcanic forcing is parameterized in this simulation as a simple reduction of the annual-mean solar constant, starting in the year with a volcanic eruption and usually lasting a couple of years, according to the reconstructions of volcanic aerosol forcing (Crowley 2000). This second experiment includes the major natural and anthropogenic forcings in the past millennium, but a number of other potentially important forcings (i.e., anthropogenic tropospheric sulfate aerosols, the effect of land-use and vegetation changes, and some other greenhouse gases, such as halocarbons and ozone) were excluded in the ERIK experiment. We keep in mind that the neglected anthropogenic factors may have a significant impact on the climate in the twentieth century. For example, sulfate aerosols exert a negative temperature forcing. Neglect of the tropospheric sulfate aerosols in the ERIK simulation, therefore, excluded their cooling influences on temperature, leading to excessive warming in the last 30–50 yr of the twentieth century.

The initial conditions of the ERIK simulation were taken from year 100 of the control run. Those initial conditions are, however, representative of present-day rather than preindustrial climate and the experimental design therefore included a 30-yr adjustment period during which the control run forcing was linearly reduced until it matched the forcing imposed around AD 1000, followed by a 50-yr period with fixed forcing to allow the model's climate to readjust to the modified forcing. The ERIK simulation then proceeded from the conditions at AD 1000 to AD 1990. Note that uncertainties remained unresolved with the specification of initial conditions, and that the uncertainty in the initial conditions, in turn, might cause initial climate drift that could potentially influence the relationship between applied forcing and simulated response. This issue has been recognized by the authors of the simulation and has been addressed in the comment published in the *Journal of Climate* (Fig. 1 of Zorita et al. 2007).

b. Validation of the model annual-mean precipitation and annual cycle of precipitation

To assess the performance of ECHO-G in modeling precipitation climatology, we examine the annual-mean precipitation and the leading EOF mode of the monthly-mean annual cycle. The leading EOF mode accounts for about 70% of the total annual variance and its spatial pattern can be faithfully represented by the June–

September (JJAS) minus December–March (DJFM) precipitation (Wang and Ding 2008). This solstice mode captures the major portion of the global monsoon; for simplicity, it will be referred to as the global monsoon mode.

Figure 1 compares the spatial patterns of the annual mean (Fig. 1a) and global monsoon (Fig. 1b) derived from the Climate Prediction Center (CPC) Merged Analysis of Precipitation (CMAP; Xie and Arkin 1997), ECHO-G ERIK run, and National Centers for Environmental Prediction (NCEP)-2 Reanalysis (Kanamitsu et al. 2002). The CMAP data are considered here as the observed ''ground truth.'' Pattern correlation coefficients (PCC) and root-mean-square errors (RMSE) are used to gauge the model performance. The PCC of annual-mean precipitation between ERIK and CMAP (0.87) is slightly lower than that between NCEP-2 Reanalysis and CMAP (0.89). The pattern correlation of the global monsoon mode between ERIK and CMAP (0.81) is also slightly lower than that between NCEP-2 Reanalysis and CMAP (0.85). However, the RMSE of the annual-mean precipitation and global monsoon mode between ECHO-G ERIK and CMAP are 1.09 mm day^{-1} and 1.88 mm day^{-1}, which are both smaller than those between NCEP-2 Reanalysis and CMAP data (1.16 and 2.02 mm day^{-1}). These results suggest that the simulated precipitation climatology in ERIK run is comparable to those assimilated data in NCEP-2 Reanalysis. This overall agreement adds confidence to our subsequent analysis of the centennial-scale precipitation variability using the outputs generated by the ERIK run.

While the ERIK run simulates the rainfall climatology realistically, biases do exist. It can be seen from Fig. 1a that the annual-mean precipitation has significant errors in the Asian monsoon region, subtropical South Pacific convergence zone, and South Atlantic convergence zone. The monsoonal mode has significant errors in the East Asian subtropical monsoon and the Mexican–North American monsoon regions. However, the overall model results on global scale are realistic and adequate for our study of the long-term modulations of the global monsoon system by externally imposed natural and anthropogenic forcings.

3. Temporal variation of the global monsoon precipitation

a. Defining the GM domain and indexes

The GM is the dominant mode of the annual cycle of the global tropical circulation (Wang and Ding 2008). To analyze the spatiotemporal variation of GM, the global monsoon precipitation domain and the global monsoon precipitation strength are defined here following Wang and Ding (2008). Monsoonal climate is not only characterized by annual reversal of surface winds but also by a contrasting wet summers and dry winters (Webster 1987). The global monsoon precipitation domain is defined by the region in which the annual range (AR) of precipitation exceeds 2 mm day^{-1} and the local summer precipitation exceeds 55% of annual rainfall. Here AR is defined as MJJAS precipitation minus NDJFM precipitation in the Northern Hemisphere (NH) and NDJFM minus MJJAS precipitation in the Southern Hemisphere (SH).

Figure 2 shows the global monsoon domain defined by CMAP data, which consists of 6 major monsoon regions: the Northern African (N1), Southern African (S1), Asian (N2), Australian (S2), North American (N3), and South American (S4) monsoon. Note that all these major regional monsoons involve continent–ocean contrast. There is a minor region in the central South Pacific (S3), which does not involve land–ocean thermal contrast and is a ''pure'' oceanic monsoon-like region. In the following analysis, one will find that the behavior in S3 is different from those in the other major continent–ocean monsoon regions. Therefore, we exclude S3 region in the aggregate measure of the intensities for the global monsoon and Southern Hemisphere monsoon.

The monsoon strength can be represented by the annual range of the total monsoon precipitation. Since the annual range is largely controlled by the local summer precipitation, an alternative measure of the monsoon strength is simply the local summer monsoon rainfall. Thus, a NH monsoon index (NHMI) is defined as the JJA rainfall falling in the observed NH monsoon domain including both land and ocean; a SH monsoon index (SHMI) is defined as the DJF rainfall falling in the observed SH monsoon domain, which includes southern African, Australia, and South America but not the central South Pacific. Here the DJF is the season following the NH JJA. As such, the two hemispheric monsoon indexes measure the strength of the aggregated NH and SH monsoon domains, respectively. To quantify the strength of the global monsoon, we define the global monsoon index as the sum of the two hemispheric indexes; that is, GMI = NHMI + SHMI.

The GMI is a measure of the GM strength in terms of the precipitation within the global monsoon rainy domain. Under climate change, the annual cycle of the tropical circulation is expected to change. The GM strength can faithfully reflect this change as it represents the dominant mode of the tropical circulation.

b. Centennial and millennial variations of the global monsoon indexes

Figure 3 shows the time series of the 7- and 31-yr running means of the monsoon indexes (NHMI, SHMI,

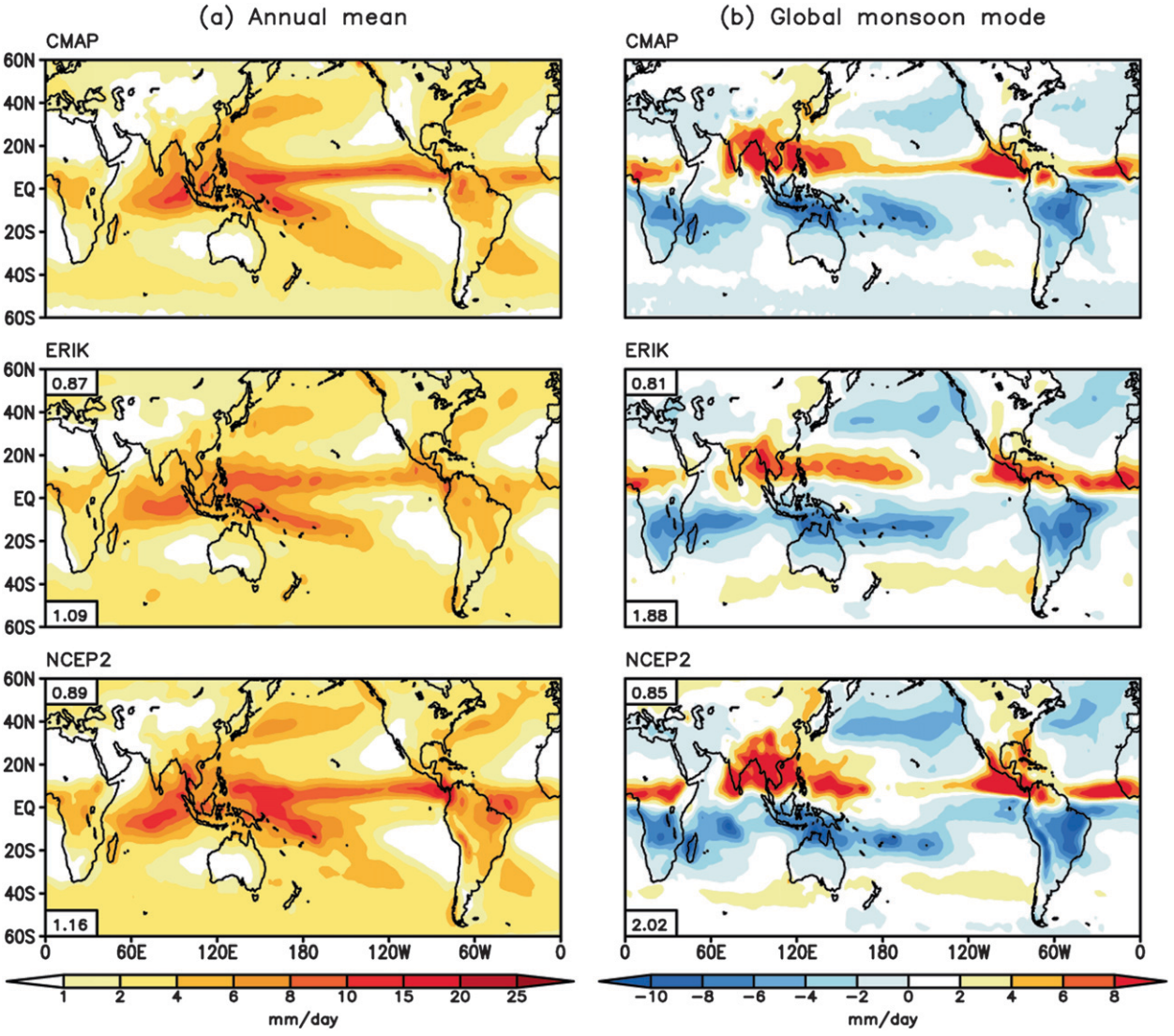

FIG. 1. Comparison of climatology of global precipitation (mm day^{-1}): (a) annual mean and (b) global monsoon mode (JJAS minus DJFM; leading EOF mode of monthly-mean annual cycle) for (top) CMAP, (middle) ECHO-G ERIK run, and (bottom) NCEP-2 Reanalysis. CMAP and NCEP-2 Reanalysis climatological data were derived for the period 1979–2004. ERIK 25-yr climatology was derived for the period AD 1965–90. The numbers shown in the upper-left corners and the lower-left corners indicate pattern correlation coefficients and RMSEs with the CMAP data, respectively.

GMI) for both the CTL (Fig. 3a) and ERIK (Fig. 3b) runs. The control run provides an opportunity to examine the internal variability due to unforced feedback processes in the coupled system. In the control run, there is no trend in NHMI, SHMI, and GMI. Furthermore, the NHMI and SHMI are not related, as evidenced by the correlation coefficients between them valued at about zero for both the 7- and 31-yr running-mean series. This result suggests a lack of coherency of the monsoon intensity between the two hemispheres without external forcing. From the observed data for the last 56 yr, it was found that the correlation coefficients between NHMI and SHMI are also very low using either the raw data or the 7-yr running-mean data (Wang and Ding 2006). But the data records are simply too short to confirm or reject any particular hypothesis concerning relation between monsoon indexes of the two hemispheres.

In the ERIK run (Fig. 3b) on the other hand, the simulated, forced responses on multidecadal scales and longer are quite different. Significant centennial variations can be seen. These variations correspond to the evolution of the global-mean temperature, where a model MWP, LIA, and PWP can be recognized (Zorita

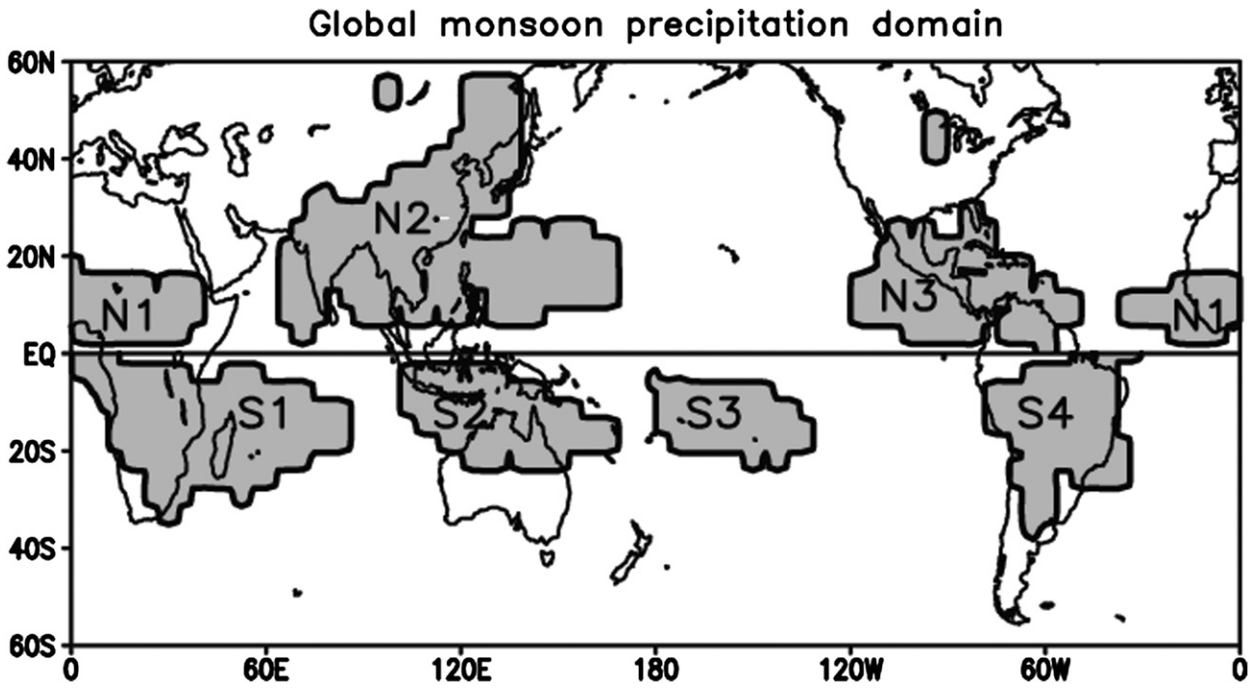

FIG. 2. The global monsoon precipitation domain defined by the region in which the AR of precipitation exceeds 2mm day^{-1} and the local summer precipitation exceeds 55% of annual rainfall by using CMAP data.

et al. 2005). According to the model simulation, strong global monsoon signal is observed around 1030–1240, which is defined here as the model Medieval Warm Period with three distinguished peaks around 1050, 1140, and 1200 (Fig. 3b). On the other hand, weak global monsoons are observed during the model Little Ice Age period from 1450 to 1850. It is of particular interest to find that during the Little Ice Age the GMI strength exhibits three minima, which occur around 1460, 1685, and 1800 (Fig. 3b). These rainfall minima fell in the Spörer Minimum (1420–1570), the Maunder Minimum (1645–1715), and the Dalton Minimum (1790–1820) periods of low sunspot activity, and in the two latter cases increased volcanic activity as well (Soon and Yaskell 2004; Haltia-Hovi et al. 2007). This suggests a connection with the centennial-scale modulation of the solar and/or volcanic radiative forcings. In sharp contrast, such historically timed GM minima were not found in the unforced CTL runs. The strengthening of modeled GM in the twentieth century and especially during the 1960–90 interval seems unprecedented, which corresponds to the sharp multidecadal increase in solar forcing during the first half of the twentieth century and the large increase in atmospheric CO_2 and CH_4 concentration since around 1800 (see further discussion in section 5 below). Additionally, the NHMI and SHMI are significantly correlated on multidecadal to centennial time scales, the correlation coefficients between them are 0.71 for 31-yr running-mean series.

Centennial variations are also significant in the ERIK run. Power spectrum analyses (Wei 2007) of the 31-yr running-mean series of the hemispheric-scale monsoon indexes (GMI, NHMI, and SHMI) for the ERIK run are shown in Fig. 4. It can be seen that a 192-yr peak is significant above 95% confidence level (by red noise test) for the global and SH monsoon indexes. The NHMI (Fig. 4b) has a less significant 192-yr peak probably because of larger random noises on this bicentennial scale in the Northern Hemisphere. Other significant periods in the GMI spectrum are marked around 107 yr (mainly because of NHMI) and 74 yr (mainly because of SHMI). We have also calculated the power spectra for all three monsoon indexes using both the raw annual data and the 7-yr running-mean data with quantitatively different spectral peaks and different statistical significances of the peaks, cautioning on the artificial effects of the real spectra convoluted with the spectra of the smoothing filter. However, we believe that the bicentennial and centennial scales in the modulated GMI, NHMI, and SHMI indexes are qualitatively robust and may be plausibly connected to the prescribed forcing and response of the global monsoon system studied here.

On the global scale, there have been no integrated observations that can be used for either checking or

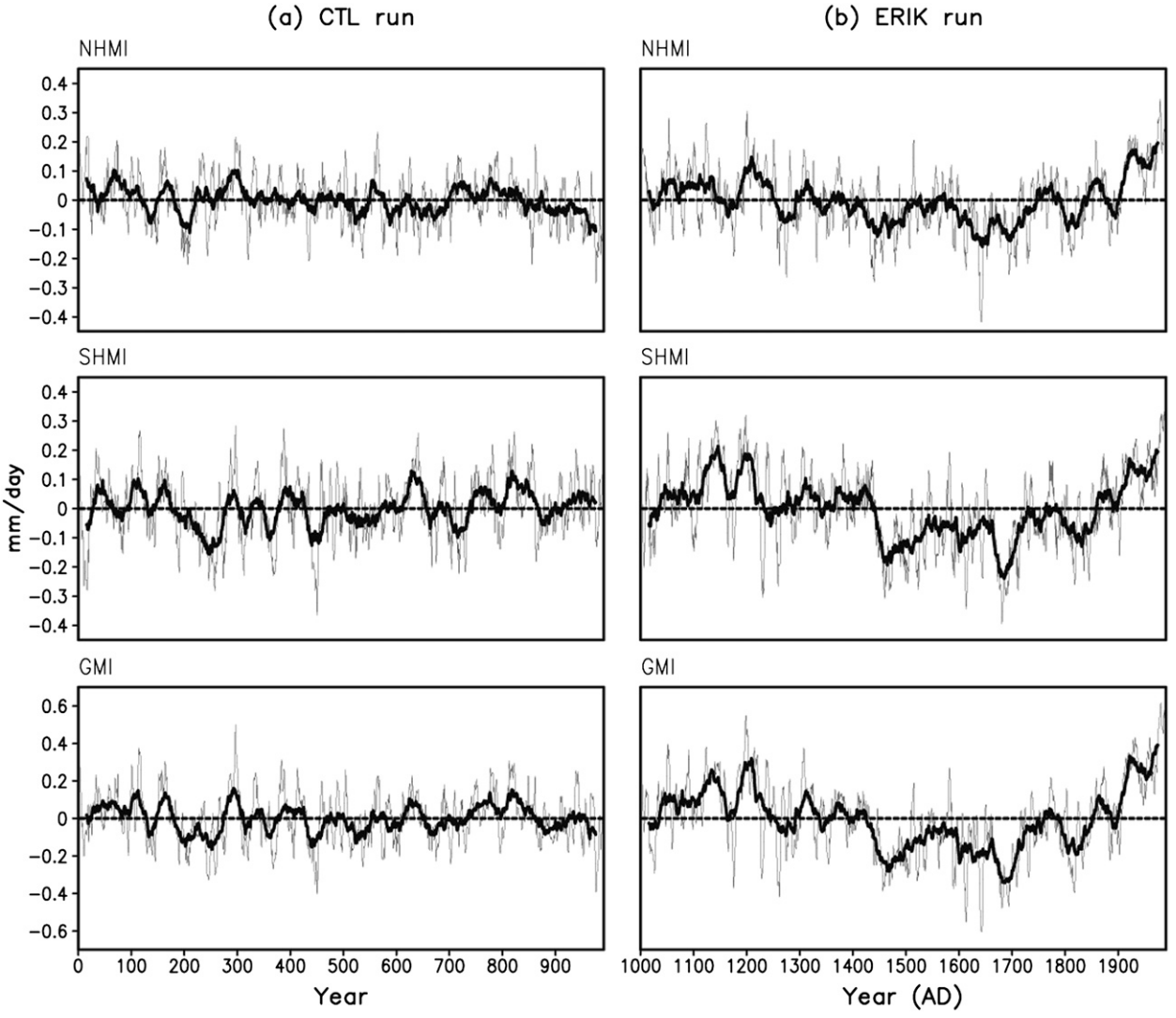

FIG. 3. Time series of the 7-yr running-mean monsoon indexes: (a) CTL (free coupled) run and (b) ERIK (forced) run for (top) NHMI, (middle) SHMI, and (bottom) GMI. The thick solid lines represent the 31-yr running means, which highlight centennial variations.

confronting the model results. However, the 200-yr oscillation has been noted empirically at many individual sites (e.g., Zhong et al. 2007; van Beynen et al. 2007; Mangini et al. 2007; Allen et al. 2007; Vonmoos et al. 2006; Wang et al. 2005; Lim et al. 2005; Holzkämper et al. 2004; Delmonte et al. 2005; Peristykh and Damon 2003; Agnihotri et al. 2002; Wagner et al. 2001; Chambers and Blackford 2001; Hong et al. 2001, 2000; Ram and Stolz 1999; Yu and Ito 1999; Leventer et al. 1996). The period of 74 yr is very significant (60~80 yr) in the South Asian and East Asian monsoon region for both temperature and precipitation (Zhu and Wang 2002; Goswami 2004; Ding et al. 2007). The ECHO-G results might provide useful clues for further assembling empirical proxy data on the global scale and for interpretation of underlying physical mechanisms to the 200-yr oscillation.

4. Variations in the spatial structure of the 30-yr climatology of the global monsoon

The spatial structure of annual-mean precipitation anomaly and the global monsoon precipitation anomaly with reference to the corresponding long-term means (1000–1990) during the three periods of MWP, LIA, and PWP are shown in Fig. 5. The annual-mean precipitation anomalies during the MWP, LIA, and PWP depict how the mean precipitations during these three epochs deviate from the long-term mean precipitation

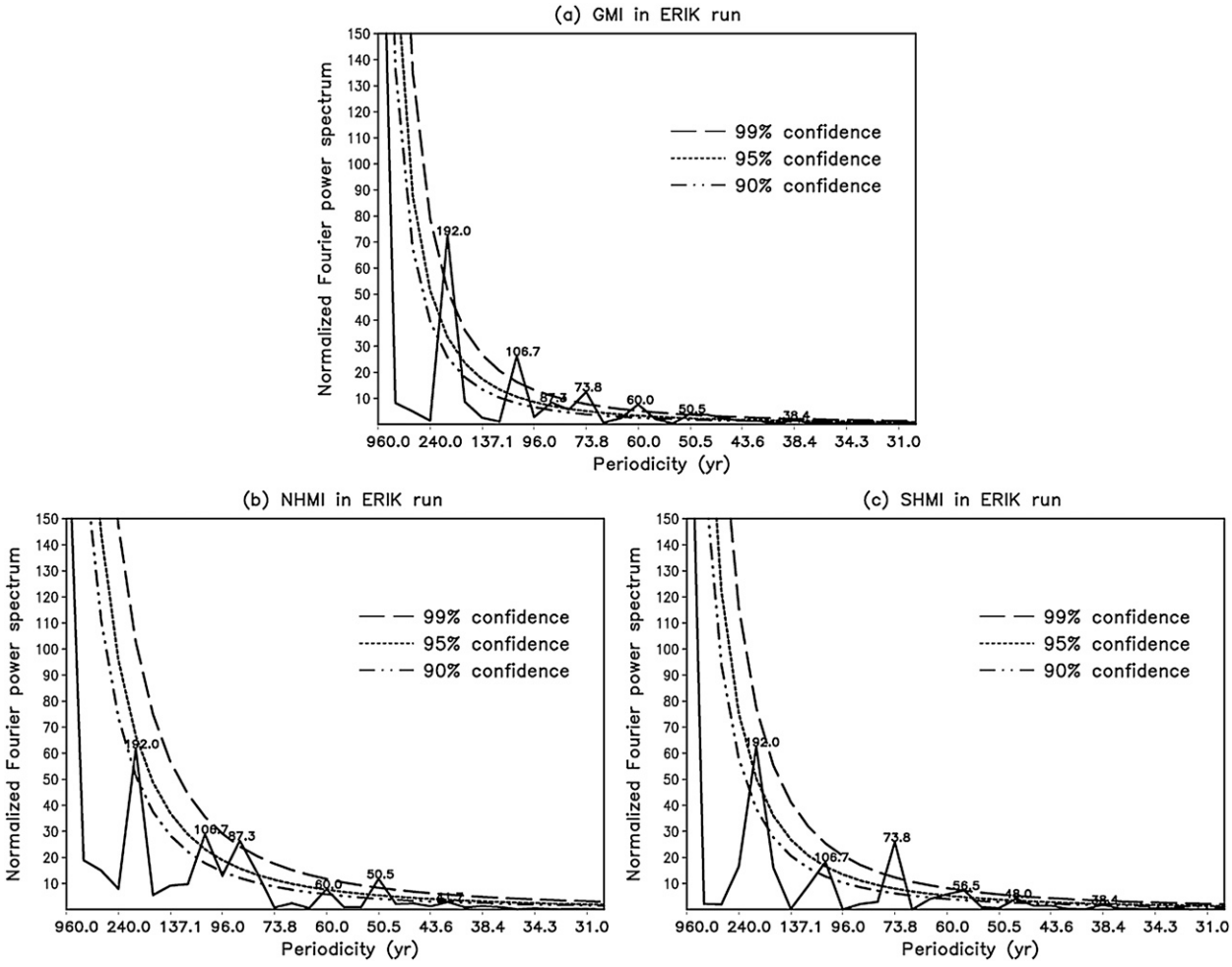

FIG. 4. Spectrum analyses on the 31-yr running mean of the monsoon indexes for ERIK simulation: (a) GMI, (b) NHMI, and (c) SHMI.

(1000–1990). Note that the global monsoon precipitation anomaly is defined by the JJA precipitation anomaly in the NH and DJF precipitation anomaly in the SH, which depicts the strength of the local summer monsoon precipitation or roughly the annual range of the monsoon precipitation. The MWP and LIA periods are plotted around the maximum of GMI intensity at 1200 and the minimum of GMI at 1685, respectively (see Fig. 3).

Figure 5a compares the annual-mean precipitation distribution for the three periods. The annual-mean precipitation between 45°S and 45°N is 3.12 mm, 3.09, and 3.12 mm day^{-1} for MWP, LIA, and PWP, respectively (Table 1), which indicates the increase of the total rainfall between 45°S and 45°N during the warm periods of MWP and PWP. The annual-mean precipitation in all the 6 continental monsoon domains is 3.78, 3.75, and 3.80 mm day^{-1} (Table 1) for MWP, LIA and PWP, respectively, which means that the annual-mean precipitation in the global monsoon domain decreased during the relatively cold LIA period compared to the MWP and PWP periods. Although with a slight difference in the timing for LIA and MWP and probably beyond the spatial resolution of our model outputs, the recent high-quality reconstruction of monsoon rainfalls for southwest China (between the moisture transport pathway of Dongge Cave and Heshang Cave; broadly represented by our N2 monsoon region) by Hu et al. (2007) suggested a relatively wetter and dryer conditions for the MWP and LIA, respectively.

Figure 5b compares the local summer precipitation changes connected to the changes in the local monsoon strength. During the MWP and PWP periods, monsoon strengthens nearly globally in each of the continental regional monsoons. This is especially so for the present-day monsoon climatology. On the other hand, during the LIA, there is a general decrease in each

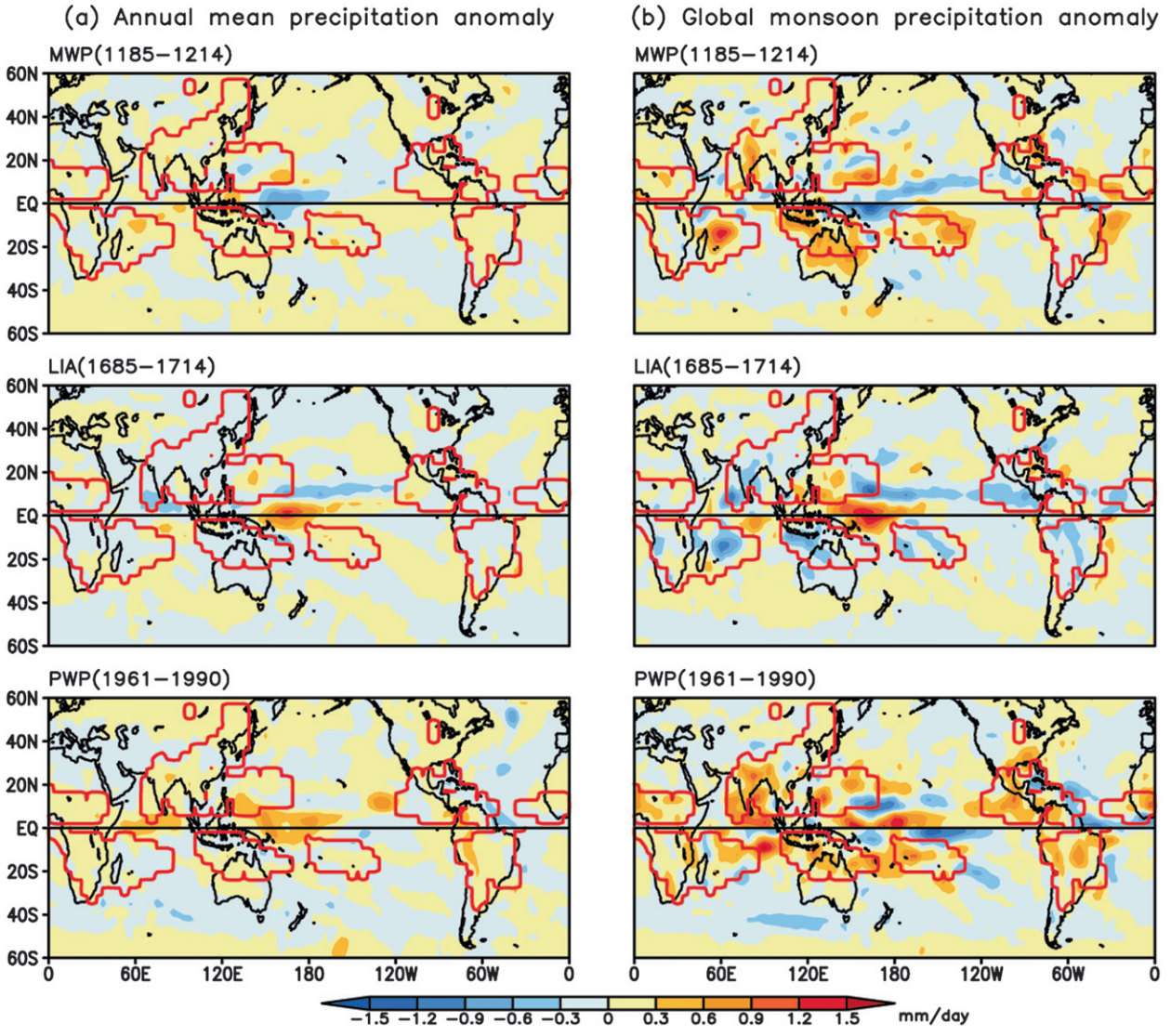

FIG. 5. Comparison of precipitation patterns for the three 30-yr epochs: (top) MWP (1185–1214), (middle) LIA (1685–1714), and (bottom) PWP (1961–90). (a) The annual-mean precipitation anomaly and (b) the global monsoon precipitation anomaly with reference to the corresponding long-term means (1000–1990). The global monsoon precipitation is defined by the JJA precipitation in the NH and DJF precipitation in the SH. The enclosed red lines outline the monsoon domains.

of the monsoon regions except the oceanic S3. The precipitation anomaly of global monsoon during the MWP, LIA, and PWP is 0.014, −0.021, and 0.029 mm day^{-1}, respectively. This fact suggests that forced responses of the regional monsoons have a cohesive pattern and they are coordinated by the superposed changes in the external forcing. Thus, the global monsoon index offers the measure of a global-scale trend common to the regional monsoons except oceanic monsoon region S3.

We next note that, although the increase in GMI is similar between MWP and PWP, the spatial patterns have some differences (Fig. 5b). The present-day climate features largest increase of the annual-mean precipitation over the equatorial western Pacific, while during MWP rainfall over the equatorial western Pacific warm pool decreases significantly. Changes in the monsoon strength in the Mexican monsoon also differ significantly for the simulated monsoon climatologies for the MWP and PWP.

Table 1 shows that the oceanic monsoon S3 behaves differently from all other 6 continental monsoon regions. In the continental monsoon regions, LIA precipitation is less than MWP and PWP period, but the oceanic

TABLE 1. The annual-mean precipitation (mm day^{-1}) of regional and global monsoon regions (exclude S3) and 45°N–45°S belt during the MWP (1185–1214), LIA (1685–1714), and PWP (1961–90). The notation N1, N2, N3, S1, S2, S3, and S4 represents the northern African, Asian, North American, Southern African, Australian, central South Pacific, and South American monsoon regions, respectively.

Region	MWP	LIA	PWP
N1	3.187	3.181	3.285
N2	3.734	3.642	3.790
N3	5.108	5.047	5.056
S1	3.463	3.334	3.408
S2	3.599	3.405	3.473
S3	6.088	6.137	6.087
S4	3.885	3.832	3.985
Global monsoon (without S3)	3.782	3.747	3.798
45°N–45°S belt	3.122	3.092	3.117

monsoon region (S3) is just opposite. For this reason, we had excluded S3 from our integrated monsoon indexes, namely the SHMI and GMI.

5. Attribution and mechanisms

Figure 6 compares the time series of the direct solar radiative forcing, indirect radiative forcing from volcanic eruptions, effective radiation forcing (the sum of the solar and volcanic forcing), and atmospheric CO_2 concentration, along with the global monsoon index, global-mean temperature, and interhemispheric temperature difference (NH minus SH). All time series were smoothed with a 31-yr running-mean filter in order to better highlight centennial-to-millennial variations. The correlation coefficients between GMI and the suspected relational or causal factors are shown in the lower-right corners of Fig. 6 and presented in greater details in Table 2.

a. Variations of the forcing factors

The amplitude of variations of the solar irradiance at centennial and longer time scales is still being debated (Krivova et al. 2007; Solanki and Krivova 2006; Bard and Frank 2006). The amplitude of these variations is usually scaled numerically by the difference between present values and the Late Maunder Minimum. In this simulation this difference (1960–90 mean minus 1680–1710 mean) is 0.3%. Thus, in the simulation the solar radiation reaching the top of the atmosphere shows significant variation on millennium time scale with a maximum around 1100–1250 and the present day together with a minimum around 1450 (Fig. 6a). The latest value in the simulation (1990) is about 1 W m^{-2} higher

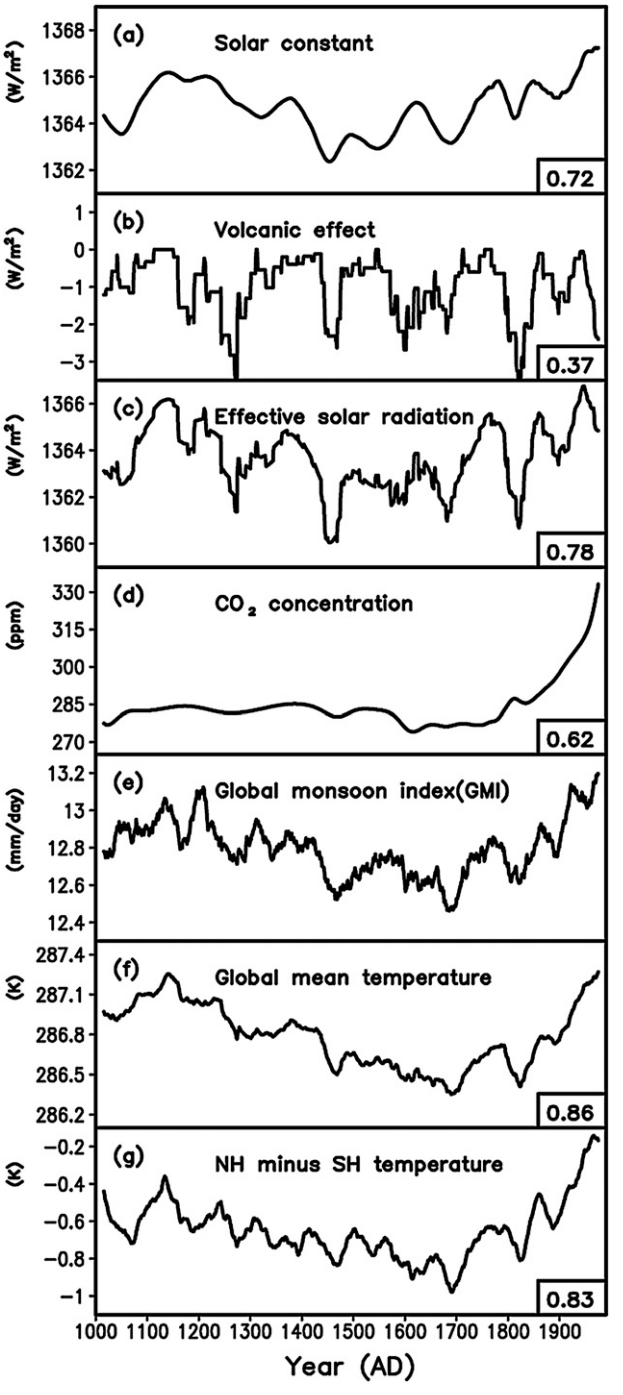

FIG. 6. Smoothed time series of the (a) solar radiative forcing (W m^{-2}), (b) volcanic effect (W m^{-2}), (c) effective solar radiation (W m^{-2}), (d) CO_2 concentration (ppm), (e) GMI (mm day^{-1}), (f) global-mean temperature (K), and (g) interhemispheric temperature difference (K). All time series are 31-yr running means from AD 1000 to 1990. The numbers shown in the lower-right corners indicate correlation coefficients of GMI with the four external forcing factors and two temperature indexes, respectively. The interhemispheric temperature difference is defined by the NH averaged temperature minus the SH averaged temperature.

TABLE 2. Correlation coefficients between GMI and other variables in ERIK run. Those values that are statistically significant at the 95% confidence level are indicated in bold numbers. The method of significant test follows Chen (1982).

Correlation coefficient	Solar constant	Volcanic activity	Effective solar radiation	CO_2	CH_4	Global-mean temperature	NH−SH temperature
Original data	0.328	**0.245**	**0.335**	**0.294**	0.251	**0.382**	**0.427**
7-yr running mean	0.579	**0.384**	**0.638**	**0.518**	**0.438**	**0.724**	**0.659**
31-yr running mean	0.724	**0.374**	**0.777**	**0.618**	0.500	**0.862**	**0.834**

than the MWP period. There are centennial fluctuations superposed on the millennium variation. Spectral analysis shown in Fig. 7a confirms that the variance is concentrated on centennial and bicentennial time scales and with prominent peaks occurring on 192 and 120 yr. Similar to our calculations of the power spectra for the monsoonal indexes in Fig. 4, we have also found quantitatively different results for both the peaks and their statistical significances for all the indexes in Fig. 7 using both the raw annual-mean and the 7-yr smoothed series. We believe that these quantitative differences will not strongly affect the key conclusion in the narrow context of our study of the bicentennial and centennial scales of forcing and response of the global monsoon system.

The episode of volcanic forcing changes from year to year; its 31-yr running mean shows primarily a variation on bicentennial time scales (Fig. 6b). The spectral analysis confirms peaks on 192 and 107 yr, respectively, which are both significant at the 95% confidence level (Fig. 7b). What gives rise to the periodicity in the effective volcanic forcing is very curious because volcanic eruptions have been thought to be more or less chaotic and unpredictable with no regularity in time.

The effective solar forcing reaching the top of the atmosphere, which is the sum of the solar forcing at the top of the atmosphere and the radiative equivalent of volcanic activity, shows both a long-term variation (presumably on a millennial time scale owing mainly to the variation of the solar radiation) and quasi-bicentennial (192 yr) and quasi-centennial (107 yr) variations (primarily due to the superposed variations of both the volcanic and solar forcings; see Figs. 6c and 7c). These spectral peaks are significant at the 99% confidence level by red noise test, but we rather place emphasis on physical mechanisms than statistics.

The atmospheric CO_2 concentration in the preindustrial period is flat (around 285 ppm) except a relatively low period between 1600 and 1800 (i.e., at about 275–280 ppm; see Fig. 6d). The smoothed CO_2 series has increased near exponentially since 1850–1975 (around 330 ppm). Atmospheric CH_4 is also important, for it is responsible for about 25% of the increase anthropogenic radiative forcing between preindustrial period and the present (Solomon et al. 2007).

b. *Response of the global monsoon precipitation to external forcing*

How does the global monsoon precipitation respond to the changes in the aforementioned forcings? Fig. 6e shows that the GMI tends to vary in phase with the effective radiative shortwave forcing (solar forcing plus volcanic forcing), especially on the millennium time scales. The correlation coefficient between GMI and the effective radiation is 0.78 for the 31-yr smoothed series, which is slightly better than the correlation with the solar forcing (0.72) and much better than the correlation with the volcanic forcing (0.37; see Fig. 6 and Table 2). The better correlation between the GMI and solar forcing comes from their millennium variations. The spectrum of the GMI has pronounced peaks on 192, 107, and 74 yr (Fig. 7d), which corresponds well to the significant spectral peaks from effective radiative forcing at around 192, 107, and 80 yr.

The variation of the GM precipitation may thus be linked to three factors. First, its millennium variation (peaks in MWP and present and dips in LIA interval) can be well explained by changes in the direct solar irradiance. The three GMI minima during the LIA concur with the three minima in shortwave forcing, which further supports the impact of the effective solar forcing on the global monsoon precipitation. Second, a comparison of Figs. 7a–c with Fig. 7d suggests that the quasi-bicentennial (192 yr) oscillations in the GM precipitation appear to be primarily induced by the solar forcing with amplification by the volcanic forcing. The quasi-centennial (107 yr) oscillation may be related primarily to volcanic forcing with amplification by the solar forcing. Third, while the direct solar irradiance in the last two decades of the simulation is higher than that of MWP by about 1 W m^{-2}, the effective solar irradiance in the late twentieth century is 0.52 W m^{-2} lower than that during MWP because of the increase in effective volcanic forcing in the late twentieth century (see Fig. 6). On the other hand, the GM rainfall rate in the PWP is 0.016 mm day^{-1} higher than that during the

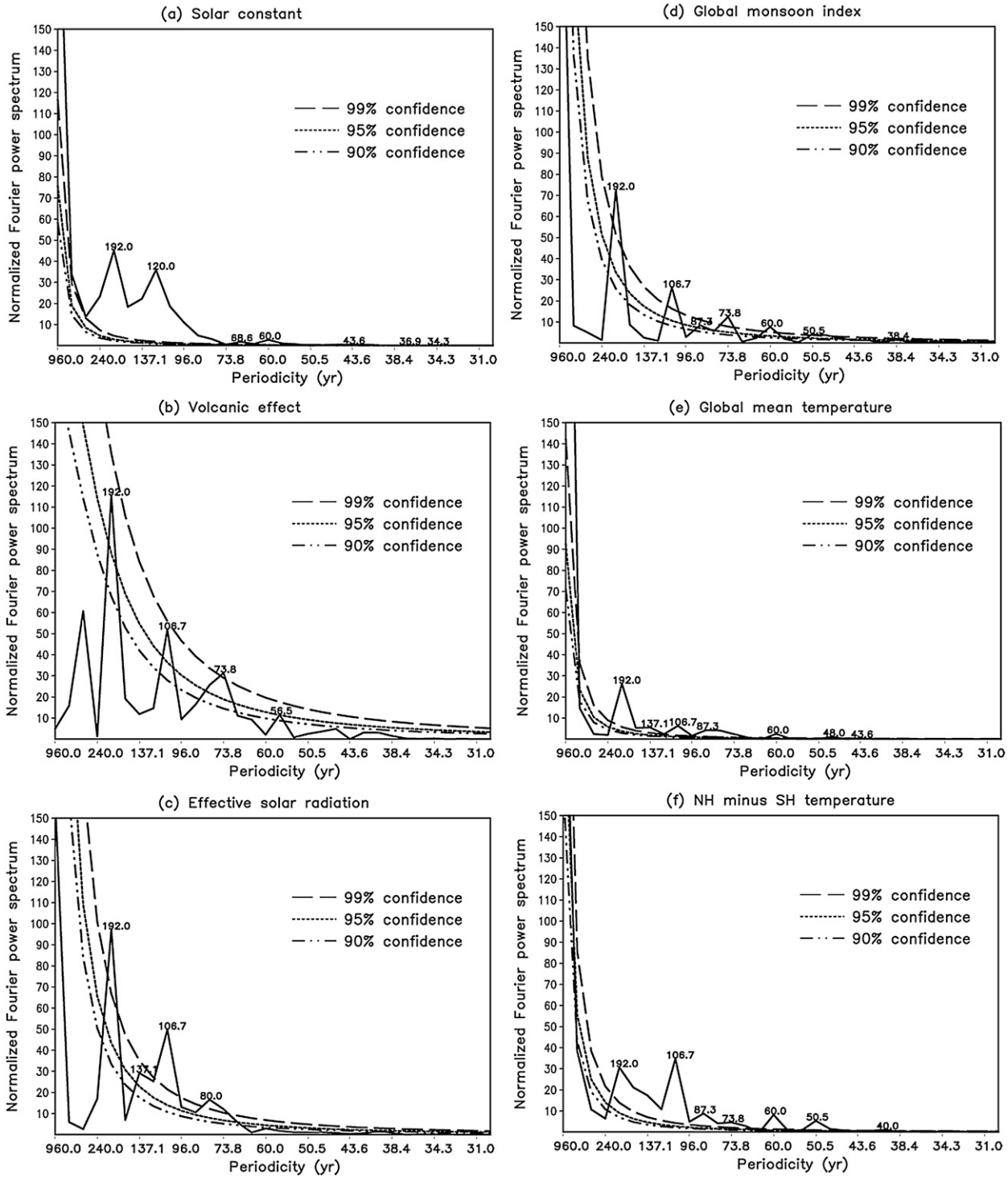

FIG. 7. Spectra of the 31-yr running-mean external forcing factors and atmospheric responses. (a) Solar constant, (b) volcanic effect, (c) effective solar radiation, (d) GMI, (e) global-mean temperature, (f) NH minus SH temperature.

MWP (Table 1), which indicates that the solar and volcanic forcing can explain the simulated GM rainfall from 1000 to 1950, but fails to account for most of the observed increase of GM precipitation in 1961–90, especially after 1975. This fact may suggest that the rapid increase of atmospheric CO_2 and CH_4 might have a positive contribution to the recent increase in the GM precipitation.

c. The mechanism by which effective radiative forcing modulates GM rainfall

In the preindustrial period, changes in the total amount of effective shortwave radiative forcing can reinforce the thermal contrast between the continent and ocean, thereby resulting in the centennial- to millennial-scale variations in the global monsoon strength. Land has much smaller heat capacity than the ocean. When effective radiative flux increases during the local summer, the magnitude of land warming is much stronger than that in the adjacent ocean, thus the thermal contrast between continent and ocean gets reinforced (Table 3). This thermal contrast further enhances the pressure differences between land monsoon regions and the surrounding oceans (Table 3) and thus strengthens the monsoon circulation in the presence of Coriolis force and associated rainfall. As such, each regional component of the global monsoon system will intensify from the increased radiative heating and thus the composite global monsoon will be strengthened as well.

Quantitatively, the change in GM rainfall rate between MWP and LIA is about 0.035 mm day^{-1}, which is about 0.93% change in precipitation strength (Table 1), while the change of solar irradiance between MWP and LIA is about 2.71 W m^{-2} (Table 3), which is about 0.2% of the solar constant. Given a 0.2% increase in the external forcing, the increase in GM rainfall is 4–5 times larger. Such amplified response is similar to a near-resonant response of a dynamical system to an external forcing. What processes have catalyzed and amplified the response? We argue that the effective radiative forcing-induced land–ocean thermal contrast causes an initial increase in monsoon precipitation. This initial increase is further reinforced by the increase in moisture supply because the warming induced by the effective radiative heating tends to increase atmospheric moisture content. The increase of moisture supply can induce a positive feedback between the latent heat release (in precipitation) and monsoon flow convergence, thus further amplify the latent heating release, which may ultimately amplify the atmospheric circulation response. Therefore, the humidity feedback is a key amplifier linking solar irradiance and monsoon. A vigorous increase in rainfall is expected in response to a moderate change in radiative heating.

d. Relationship between changes in global temperature and monsoon rainfall

It can be observed from the results in Fig. 6 and Table 2 that the change of the global monsoon strength tends to roughly vary in accord to the changes in the global-mean surface temperature. The correlation coefficient between the 31-yr running-mean GMI and global-mean temperature is 0.86. However, the global monsoon rainfall follows effective radiative forcing more closely than the global-mean temperature does. This point is particularly well fulfilled during the LIA (Figs. 6c,e,f). Overall, the correlation coefficient between the 31-yr running-mean GMI and effective solar radiation is 0.78, while that between global-mean temperature and effective solar radiation is 0.69.

TABLE 3. The anomalies of effective solar radiation (ΔS) and summer mean (JJA for NH and DJF for SH) differences of sea level pressure and temperature between land and sea for MWP, LIA, and PWP intervals in reference to 1000–1990. The difference between the land and ocean was computed based on the averaged quantity over all land grids minus that over all oceanic grids.

Increment		MWP	LIA	PWP
ΔS (w m^{-2})		1.576	−1.138	1.052
90°N–0°	$\Delta(P_{sea}-P_{land})$ (hPa)	0.273	−0.150	0.309
	$\Delta T_{land}-\Delta T_{sea}$ (K)	0.080	−0.137	0.217
90°S–0°	$\Delta(P_{sea}-P_{land})$ (hPa)	0.457	−0.307	0.779
	$\Delta T_{land}-\Delta T_{sea}$ (K)	0.016	−0.078	0.147

The global monsoon is essentially driven by the interhemispheric temperature difference and differential heating between the NH and SH. To understand the changes in the global monsoon strength or GMI, one should naturally seek for the root cause from the interhemispheric contrast in the temperature and precipitation. It is found that the GMI varies coherently with the interhemispheric temperature difference. The variation of the interhemispheric temperature difference has 192- and 107-yr periodicities; both are significant above 99% confidence level (Fig. 7f). This result means that the quasi-bicentennial and quasi-centennial GM changes coherently with the interhemispheric temperature difference. The interhemispheric temperature difference is related to the solar activity change and the land–ocean distribution. Poleward of 20°N, earth's surface is covered largely by land and the proportion of land there is 47%. In contrast, poleward of 20°S, land proportion is much smaller (only 26%). In response to increased radiative forcing, the NH warms up more than the SH because of the smaller heat capacity of land. As such, the NH minus SH temperature should vary in concert with the effective radiative forcing, and is thus correlated closely with the GM precipitation changes.

6. Conclusions

In this paper, we study how the global monsoon (GM) precipitation responds to the external forcing in the last millennium by analyzing a pair of control and forced millennium simulations. The forced ERIK run has been

shown to capture precipitation climatology realistically (Fig. 1) despite the incomplete accounting of all forcing factors. More specifically, two variables are used to gauge the model's performance in simulation of the precipitation. One is the global-mean precipitation and the other is the leading mode of the annual cycle of precipitation. The leading mode of the annual cycle is characterized by a solstitial monsoonal mode whose strength can be described by a global monsoon precipitation index. We demonstrate that the ERIK run captures the two modes of climatology comparably well when compared with those captured by the NCEP reanalysis. This adds confidence to the analysis of the change in the annual cycle in the model's millennium simulation.

The 31-yr running averaged global monsoon index in the forced run reveals both the variability on the millennial time scale and significant quasi-bicentennial (192 yr) and quasi-centennial (107 yr) variability. Over the past millennium, the simulated global monsoons are observed to be strong in the model Medieval Warm Period (ca. 1030–1240), while the simulated global monsoon intensity gets weaker during the model Little Ice Age (ca. 1450–1850). During the LIA interval there are three GMI minima occurring around 1460, 1685, and 1800, which correspond, respectively, to the Spörer Minimum (1420–1570), Maunder Minimum (1645–1715), and Dalton Minimum (1790–1820) periods of solar activity minima and increased volcanic activity. The prominent increase of the global monsoon strength in the last century and the remarkably strengthening of the global monsoon in the last 30 yr of simulation ending in 1990 seem large; the latter may signify a possible impact from the rapid increase in atmospheric greenhouse gases.

Before the industrial period, the changes in the sum of the direct solar radiative forcing and volcanic forcing (effective radiative forcing) can explain the natural global monsoon precipitation variations well. Simulated changes of the GM strength in the last century have a spatial pattern that differs from that during the MWP, suggesting the different effects of global warming on monsoon precipitation patterns contributed by both the increases of atmospheric greenhouse gases and the incoming solar radiation.

On a centennial time scale, the change of the global monsoon strength follows the effective radiative forcing better than the changes of the global-mean surface temperature. Physically, the GMI has a good correlation with interhemispheric temperature difference as elaborated in the previous section.

We leave two main areas of research for future attention in order to bring forth a more complete characterization and understanding of global monsoon and its variation on centennial to millennial time scales. First, a more complete set of relevant forcing factors and physical processes must be included in the model simulation. Then a more direct and meaningful comparison of the model simulated outputs with all the available regional monsoon proxies can be performed.

Acknowledgments. Jian Liu and Bin Wang acknowledge the financial supports from the Innovation Project of Chinese Academy of Sciences (Grant KZCX2-YW-315),the National Basic Research Program of China (Grant 2004CB720208), and the National Natural Science Foundation of China (Grant 40672210). Bin Wang and Qinghua Ding acknowledge the support received from the National Science Foundation (NSF) climate dynamics program (ATM06-29531) and NOAA/OGP.

REFERENCES

Agnihotri, R., K. Dutta, R. Bhushan, and B. L. K. Somayajulu, 2002: Evidence for solar forcing on the Indian monsoon during the last millennium. *Earth Planet. Sci. Lett.,* **198,** 521–527.

Allen, J. R. M., A. J. Long, C. J. Ottley, D. G. Pearson, and B. Huntley, 2007: Holocene climate variability in northernmost Europe. *Quat. Sci. Rev.,* **26,** 1432–1453.

Ammann, C. M., F. Joos, D. S. Schimel, B. L. Otto-Bliesner, and R. A. Tomas, 2007: Solar influence on climate during the past millennium: Results from transient simulations with the NCAR Climate System Model. *Proc. Natl. Acad. Sci. USA,* **104,** 3713–3718.

Bard, E., and M. Frank, 2006: Climate change and solar variability: What's new under the sun? *Earth Planet. Sci. Lett.,* **248,** 1–14.

Bauer, E., M. Claussen, V. Brovkin, and A. Huenerbein, 2003: Assessing climate forcings of the earth system for the past millennium. *Geophys. Res. Lett.,* **30,** 1276, doi:10.1029/2002GL016639.

Beltrami, H., J. F. González-Rouco, and M. B. Stevens, 2006: Subsurface temperatures during the last millennium: Model and observation. *Geophys. Res. Lett.,* **33,** L09705, doi:10.1029/2006GL026050.

Blunier, T., J. Chappellaz, J. Schwander, B. Stauffer, and D. Raynaud, 1995: Variations in atmospheric methane concentration during the Holocene epoch. *Nature,* **374,** 46–49.

Chambers, F. M., and J. J. Blackford, 2001: Mid- and late-Holocene climatic changes: A test of periodicity and solar forcing in proxy-climate data from blanket peat bogs. *J. Quat. Sci.,* **16,** 329–338.

Chen, W. Y., 1982: Fluctuations in Northern Hemisphere 700 mb height field associated with the Southern Oscillation. *Mon. Wea. Rev.,* **110,** 808–832.

Crowley, T. J., 2000: Causes of climate change over the past 1000 years. *Science,* **289,** 270–277.

Delmonte, B., J. R. Petit, G. Krinner, V. Maggi, J. Jouzel, and R. Udisti, 2005: Ice core evidence for secular variability and 200-year dipolar oscillations in atmospheric circulation over east Antarctica during the Holocene. *Climate Dyn.,* **24,** 641–654.

Ding, Y., Z. Wang, and Y. Sun, 2007: Inter-decadal variation of the summer precipitation in East China and its association with decreasing Asian summer monsoon. Part I: Observed evidences. *Int. J. Climatol.,* **28,** 1139–1161.

Etheridge, D. M., L. P. Steele, R. L. Langenfelds, R. J. Francey, J.-M. Barnola, and V. I. Morgan, 1996: Natural and anthropogenic changes in atmospheric CO_2 over the last 1000 years from air in Antarctic ice and firn. *J. Geophys. Res.,* **101,** 4115–4128.

Fleitmann, D., S. J. Burns, M. Mudelsee, U. Neff, J. Kramers, A. Mangini, and A. Matter, 2003: Holocene forcing of the Indian monsoon recorded in a stalagmite from southern Oman. *Science,* **300,** 1737–1739.

González-Rouco, F., H. von Storch, and E. Zorita, 2003: Deep soil temperature as proxy for surface air-temperature in a coupled model simulation of the last thousand years. *Geophys. Res. Lett.,* **30,** 2116, doi:10.1029/2003GL018264.

Goosse, H., and H. Renssen, 2004: Exciting natural modes of variability by solar and volcanic forcing: Idealized and realistic experiments. *Climate Dyn.,* **23,** 153–163.

——, ——, A. Timmermann, and R. S. Bradley, 2005: Internal and forced climate variability during the last millennium: A model-data comparison using ensemble simulations. *Quat. Sci. Rev.,* **24,** 1345–1360.

Goswami, B. N., 2004: Interdecadal change in potential predictability of the Indian summer monsoon. *Geophys. Res. Lett.,* **31,** L16208, doi:10.1029/2004GL020337.

Gouirand, I., A. Moberg, and E. Zorita, 2007a: Climate variability in Scandinavia for the past millennium simulated by an atmosphere-ocean general circulation model. *Tellus,* **59A,** 30–49.

——, V. Moron, and E. Zorita, 2007b: Teleconnections between ENSO and North Atlantic in an ECHO-G simulation of the 1000–1990 period. *Geophys. Res. Lett.,* **34,** L06705, doi:10.1029/2006GL028852.

Haltia-Hovi, E., T. Saarinen, and M. Kukkonen, 2007: A 2000-year record of solar forcing on varved lake sediment in eastern Finland. *Quat. Sci. Rev.,* **26,** 678–689.

Holzkämper, S., A. Mangini, C. Spötl, and M. Mudelsee, 2004: Timing and progression of the Last Interglacial derived from a high alpine stalagmite. *Geophys. Res. Lett.,* **31,** L07021, doi:10.1029/2003GL019112.

Hong, Y. T., H. B. Jiang, T. S. Liu, X. G. Qin, L. P. Zhou, J. Beer, H. D. Li, and X. T. Leng, 2000: Response of climate to solar forcing recorded in a 6000-year delta O-18 time-series of Chinese peat cellulose. *Holocene,* **10,** 1–7.

——, and Coauthors, 2001: A 6000-year record of changes in drought and precipitation in northeastern China based on a delta C-13 time series from peat cellulose. *Earth Planet. Sci. Lett.,* **185,** 111–119.

Hu, C., G. M. Henderson, J. Huang, S. Xie, Y. Sun, and K. R. Johnson, 2007: Quantification of Holocene Asian monsoon rainfall from spatially separated cave records. *Earth Planet. Sci. Lett.,* **266,** 221–232.

Johns, T. C., R. E. Carnell, J. F. Crossley, J. M. Gregory, J. F. B. Mitchell, C. A. Senior, S. F. B. Tett, and R. A. Wood, 1997: The second Hadley Centre coupled ocean–atmosphere GCM: Model description, spinup and validation. *Climate Dyn.,* **13,** 103–134.

Kanamitsu, M., W. Ebisuzaki, J. Woollen, S. K. Yang, J. J. Hnilo, M. Fiorino, and G. L. Potter, 2002: NCEP–DOE AMIP-II Reanalysis (R-2). *Bull. Amer. Meteor. Soc.,* **83,** 1631–1643.

Kitoh, A., 2006: Variability of Indian monsoon-ENSO relationship in a 1000-year MRI-CGCM2.2 simulation. *Nat. Hazards,* **42,** 261–272.

Krivova, N. A., L. Balmaceda, and S. K. Solanki, 2007: Reconstruction of solar total irradiance since 1700 from the surface magnetic flux. *Astron. Astrophys.,* **467,** 335–346.

Legutke, S., and R. Voss, 1999: The Hamburg Atmosphere-Ocean Coupled Circulation Model ECHO-G. German Climate Computer Center (DKRZ) Tech. Rep. 18, 62 pp.

Leventer, A., E. W. Domack, S. E. Ishman, S. Brachfeld, C. E. McClennen, and P. Manley, 1996: Productivity cycles of 200-300 years in the Antarctic Peninsula region: Understanding linkages among the sun, atmosphere, oceans, sea ice, and biota. *Geol. Soc. Amer. Bull.,* **108,** 1626–1644.

Lim, J., E. Matsumoto, and H. Kitagawa, 2005: Eolian quartz flux variations in Cheju Island, Korea, during the last 6500 yr and a possible Sun-monsoon linkage. *Quat. Res.,* **64,** 12–20.

Liu, J., H. Storch, X. Chen, E. Zorita, J. Y. Zheng, and S. Wang, 2005: Simulated and reconstructed winter temperature in the eastern China during the last millennium. *Chin. Sci. Bull.,* **50,** 2872–2877.

Manabe, S., and R. J. Stouffer, 1993: Century-scale effects of increased atmospheric CO_2 on the ocean–atmosphere system. *Nature,* **364,** 215–218.

Mangini, A., P. Verdes, C. Spötl, D. Scholz, N. Vollweiler, and B. Kromer, 2007: Persistent influence of the North Atlantic hydrography on central European winter temperature during the last 9000 years. *Geophys. Res. Lett.,* **34,** L02704, doi:10.1029/2006GL028600.

Mann, M. E., M. A. Cane, S. E. Zebiak, and A. Clement, 2005a: Volcanic and solar forcing of the tropical Pacific over the past 1000 years. *J. Climate,* **18,** 447–456.

——, S. Rutherford, E. Wahl, and C. Ammann, 2005b: Testing the fidelity of methods used in proxy-based reconstructions of past climate. *J. Climate,* **18,** 4097–4107.

Min, S.-K., S. Legutke, A. Hense, and W.-T. Kwon, 2005a: Internal variability in a 1000-yr control simulation with the coupled climate model ECHO-G—I. Near-surface temperature, precipitation and mean sea level pressure. *Tellus,* **57A,** 605–621.

——, ——, ——, and ——, 2005b: Internal variability in a 1000-yr control simulation with the coupled climate model ECHO-G—II. El Niño Southern Oscillation and North Atlantic Oscillation. *Tellus,* **57A,** 622–640.

Osborn, T. J., S. C. B. Raper, and K. R. Briffa, 2006: Simulated climate change during the last 1,000 years: Comparing the ECHO-G general circulation model with the MAGICC simple climate model. *Climate Dyn.,* **27,** 185–197.

Peristykh, A. N., and P. E. Damon, 2003: Persistence of the Gleissberg 88-year solar cycle over the last ~12,000 years: Evidence from cosmogenic isotopes. *J. Geophys. Res.,* **108,** 1003, doi:10.1029/2002JA009390.

Ram, M., and M. R. Stolz, 1999: Possible solar influences on the dust profile of the GISP2 ice core from central Greenland. *Geophys. Res. Lett.,* **26,** 1043–1046.

Rodgers, K. B., P. Friederichs, and M. Latif, 2004: Tropical Pacific decadal variability and its relation to decadal modulations of ENSO. *J. Climate,* **17,** 3761–3774.

Roeckner, E., and Coauthors, 1996: The atmospheric general circulation model ECHAM4: Model description and simulation of present-day climate. Max Planck Institute for Meteorology Tech. Rep. 218, 90 pp.

Solanki, S. K., and N. A. Krivova, 2006: Solar variability of possible relevance for planetary climates. *Space Sci. Rev.,* **125,** 25–37.

Solomon, S., and Coauthors, 2007: *Climate Change 2007: The Physical Science Basis*. Cambridge University Press, 996 pp.

Soon, W. W.-H., and S. H. Yaskell, 2004: *The Maunder Minimum and the Variable Sun-Earth Connection*. World Scientific, 296 pp.

Stendel, M., I. A. Mogensen, and J. H. Christensen, 2006: Influence of various forcings on global climate in historical times using a coupled atmosphere–ocean general circulation model. *Climate Dyn.,* **26,** 1–15.

Stouffer, R. J., G. Hegerl, and S. Tett, 2000: A comparison of surface air temperature variability in three 1000-yr coupled ocean–atmosphere model integrations. *J. Climate,* **13,** 513–537.

Tett, S. F. B., and Coauthors, 2007: The impact of natural and anthropogenic forcings on climate and hydrology since 1550. *Climate Dyn.,* **28,** 3–34.

Trenberth, K. E., D. P. Stepaniak, and J. M. Caron, 2000: The global monsoon as seen through the divergent atmospheric circulation. *J. Climate,* **13,** 3969–3993.

van Beynen, P. E., Y. Asmerom, V. Polyak, L. Soto, and J. S. Polk, 2007: Variable intensity of teleconnections during the late Holocene in subtropical North America from an isotopic study of speleothem from Florida. *Geophys. Res. Lett.,* **34,** L18703, doi:10.1029/2007GL031046.

Vimont, D. J., D. S. Battisti, and A. C. Hirst, 2002: Pacific interannual and interdecadal equatorial variability in a 1000-yr simulation of the CSIRO coupled general circulation model. *J. Climate,* **15,** 160–178.

Vonmoos, M., J. Beer, and R. Muscheler, 2006: Large variations in Holocene solar activity: Constraints from 10Be in the Greenland Ice Core Project ice core. *J. Geophys. Res.,* **111,** A10105, doi:10.1029/2005JA011500.

von Storch, H., E. Zorita, J. M. Jones, Y. Dimitriev, F. González-Rouco, and S. F. B. Tett, 2004: Reconstructing past climate from noisy data. *Science,* **306,** 679–682.

Wagner, G., and Coauthors, 2001: Presence of the solar de Vries cycle (~205 years) during the last ice age. *Geophys. Res. Lett.,* **28,** 303–306.

Wagner, S., S. Legutke, and E. Zorita, 2005: European winter temperature variability in a long coupled model simulation: The contribution of ocean dynamics. *Climate Dyn.,* **25,** 37–50.

Wang, B., 1994: Climatic regimes of tropical convection and rainfall. *J. Climate,* **7,** 1109–1118.

——, 2006: *The Asian Monsoon*. Springer, 787 pp.

——, and Q. Ding, 2006: Changes in global monsoon precipitation over the past 56 years. *Geophys. Res. Lett.,* **33,** L06711, doi:10.1029/2005GL025347.

——, and ——, 2008: Global monsoon: Dominant mode of annual variations in the tropics. *Dyn. Atmos. Oceans,* **44,** 165–183.

Wang, Y. J., and Coauthors, 2005: The Holocene Asian monsoon: Links to solar changes and North Atlantic climate. *Science,* **308,** 854–857.

Weber, S. L., T. J. Crowley, and G. van der Schrier, 2004: Solar irradiance forcing of centennial climate variability during the Holocene. *Climate Dyn.,* **22,** 539–553.

Webster, P. J., 1987: The variable and interactive monsoon. *Monsoons,* J. S. Fein and P. L. Stephens, Eds., Wiley, 269–330.

Wei, F., 2007: *Modern Techniques on Climatic Statistics, Diagnostics and Forecast* (in Chinese). China Meteorological Press, 296 pp.

Wiles, G. C., R. D. D'Arrigo, R. Villalba, P. E. Calkin, and D. J. Barclay, 2004: Century-scale solar variability and Alaskan temperature change over the past millennium. *Geophys. Res. Lett.,* **31,** L15203, doi:10.1029/2004GL020050.

Wolff, J. O., E. Maier-Reimer, and S. Legutke, 1997: The Hamburg Ocean Primitive Equation Model. German Climate Computer Center (DKRZ) Tech. Rep. 13, 98 pp.

Xie, P. P., and P. A. Arkin, 1997: Global precipitation: A 17-year monthly analysis based on gauge observations, satellite estimates, and numerical model outputs. *Bull. Amer. Meteor. Soc.,* **78,** 2539–2558.

Yu, Z. C., and E. Ito, 1999: Possible solar forcing of century-scale drought frequency in the northern Great Plains. *Geology,* **27,** 263–266.

Zhong, W., J. B. Xue, Q. Shu, and L. G. Wang, 2007: Climatic change during the last 4000 years in the southern Tarim Basin, Xinjiang, northwest China. *J. Quat. Sci.,* **22,** 659–665.

Zhu, J., and S. Wang, 2002: 80 yr oscillation of summer rainfall over North China and East Asian Summer Monsoon. *Geophys. Res. Lett.,* **29,** 1672, doi:10.1029/2001GL013997.

Zorita, E., J. F. González-Rouco, and S. Legutke, 2003: Testing the Mann et al. (1998) approach to paleoclimate reconstructions in the context of a 1000-yr control simulation with the ECHO-G coupled climate model. *J. Climate,* **16,** 1378–1390.

——, ——, H. von Storch, J. P. Montávez, and F. Valero, 2005: Natural and anthropogenic modes of surface temperature variations in the last thousand years. *Geophys. Res. Lett.,* **32,** L08707, doi:10.1029/2004GL021563.

——, ——, and ——, 2007: Comments on "Testing the fidelity of methods used in proxy-based reconstructions of past climate." *J. Climate,* **20,** 3693–3698.